

# Kinetic inductance coupling for circuit QED with spins

S. Günzler,<sup>1,2,\*</sup> D. Rieger,<sup>1,†</sup> M. Spiecker,<sup>1,2</sup> T. Koch,<sup>1</sup> G. A. Timco,<sup>3</sup>  
R. E. P. Winpenny,<sup>3</sup> I. M. Pop,<sup>1,2,4</sup> and W. Wernsdorfer<sup>1,2,‡</sup>

<sup>1</sup>*PHI, Karlsruhe Institute of Technology, 76131 Karlsruhe, Germany*

<sup>2</sup>*IQMT, Karlsruhe Institute of Technology, 76131 Karlsruhe, Germany*

<sup>3</sup>*Photon Science Institute and School of Chemistry, The University of Manchester, Manchester, UK*

<sup>4</sup>*Physics Institute 1, Stuttgart University, 70569 Stuttgart, Germany*

(Dated: February 12, 2025)

In contrast to the commonly used qubit resonator transverse coupling via the  $\sigma_{xy}$ -degree of freedom, longitudinal coupling through  $\sigma_z$  presents a tantalizing alternative: it does not hybridize the modes, eliminating Purcell decay, and it enables quantum-non-demolishing qubit readout independent of the qubit–resonator frequency detuning. Here, we demonstrate longitudinal coupling between a  $\{\text{Cr}_7\text{Ni}\}$  molecular spin qubit ensemble and the kinetic inductance of a granular aluminum superconducting microwave resonator. The inherent frequency-independence of this coupling allows for the utilization of a 7.8 GHz readout resonator to measure the full  $\{\text{Cr}_7\text{Ni}\}$  magnetization curve spanning 0–600 mT, corresponding to a spin frequency range of  $f_{\text{spin}} = 0\text{--}15$  GHz. For 2 GHz detuning from the readout resonator, we measure a  $1/e$  spin relaxation time  $\tau = 0.38$  s, limited by phonon decay to the substrate. Based on these results, we propose a path towards longitudinal coupling of single spins to a superconducting fluxonium qubit.

Spin systems are a promising platform for quantum information processing (QIP) due to their intrinsic isolation from the environment, which offers long coherence times [1–4]. However, this isolation also poses a significant challenge for spin manipulation and readout. Superconducting microwave circuits provide a compelling solution within hybrid quantum architectures [5–7], combining their versatile design, quantum-non-demolishing (QND) readout, and efficient manipulation with the long coherence times of spin systems. Over the past decade, superconducting microwave resonators have demonstrated strong coupling to spin ensembles in various systems, including vacancy centers in diamond [8], donor atoms in crystalline substrates [9–11], and molecular magnets [12–15]. Despite these achievements, inhomogeneous broadening limits ensembles coherence, and QIP requires precise control over individual spins - a milestone recently achieved through the readout and manipulation of single electron spins [4, 16].

These advances rely on transverse coupling between spins and microwave resonators. For the simplest case of a two-level spin system, the resonator microwave field couples to the spin transverse component:  $H_{\text{int}}^{\perp} = \hbar g_x \sigma_x (a^{\dagger} + a)$ , where  $g_x$  is the coupling constant,  $a^{\dagger}$  and  $a$  are the resonator bosonic operators and  $\sigma_x$  is the spin Pauli matrix. While mode hybridization due to transverse coupling enables Purcell-effect spin readout [4, 10–13, 16, 17], it is restricted to the cavity frequency and inherently non-QND [18, 19]. Longitudinal interaction provides a robust alternative because the spins couple directly to the resonator frequency via  $\sigma_z$ , i.e.  $H_{\text{int}}^{\parallel} = \hbar g_z \sigma_z a^{\dagger} a$ . The longitudinal coupling strength

$g_z = \delta\omega/2$  leads to a spin-flip induced frequency shift  $\delta\omega$ . Since  $H_{\text{int}}^{\parallel}$  commutes with  $\sigma_z$ , it mitigates the limitations of transverse coupling, enabling frequency-independent and QND readout [20–23].

We argue that kinetic inductance presents a promising platform for longitudinal spin coupling, as it can be modulated by magnetic fields or screening currents induced by nearby spins. Superconducting quantum interference devices (SQUIDs) are a potential implementation, where the spin magnetic moment tunes the SQUID critical current [15, 24] and the corresponding kinetic inductance. However, SQUID-based designs face challenges, including limited spin-flux coupling in loop geometries — preventing scalability toward single-spin readout [24] — and the intrinsic nonlinearity of Josephson junctions, which limits the power dynamic range of microwave devices. Disordered superconductors, such as NbN, NbTiN, InOx, and granular aluminum (grAl), provide a more versatile kinetic inductance for longitudinal coupling [25–32]. These materials offer several key advantages: (i) intrinsic magnetic field susceptibility without requiring a loop geometry, (ii) resilience in Tesla magnetic fields, and (iii) adaptable nonlinearity, which can be significantly lower compared to JJ-based devices [33]. While kinetic inductance magnetometers (KIMs) [34–36] represent an important step forward, the longitudinal coupling of spins to a microwave device has yet to be demonstrated.

In this work, we demonstrate longitudinal coupling between a  $\{\text{Cr}_7\text{Ni}\}$  molecular spin qubit ensemble and the kinetic inductance of a grAl microwave resonator. The spin ensemble polarization is encoded in the resonator frequency, independent of the spin-resonator detuning, enabling us to perform a full microwave readout of the magnetization curve. Moreover, we demonstrate time resolved measurement of spin ensemble excitation and decay at GHz detuning from the readout. Finally, we propose a scheme to achieve single spin longitudinal coupling

\* [simon.guenzler@kit.edu](mailto:simon.guenzler@kit.edu)

† First two authors contributed equally.

‡ [wolfgang.wernsdorfer@kit.edu](mailto:wolfgang.wernsdorfer@kit.edu)

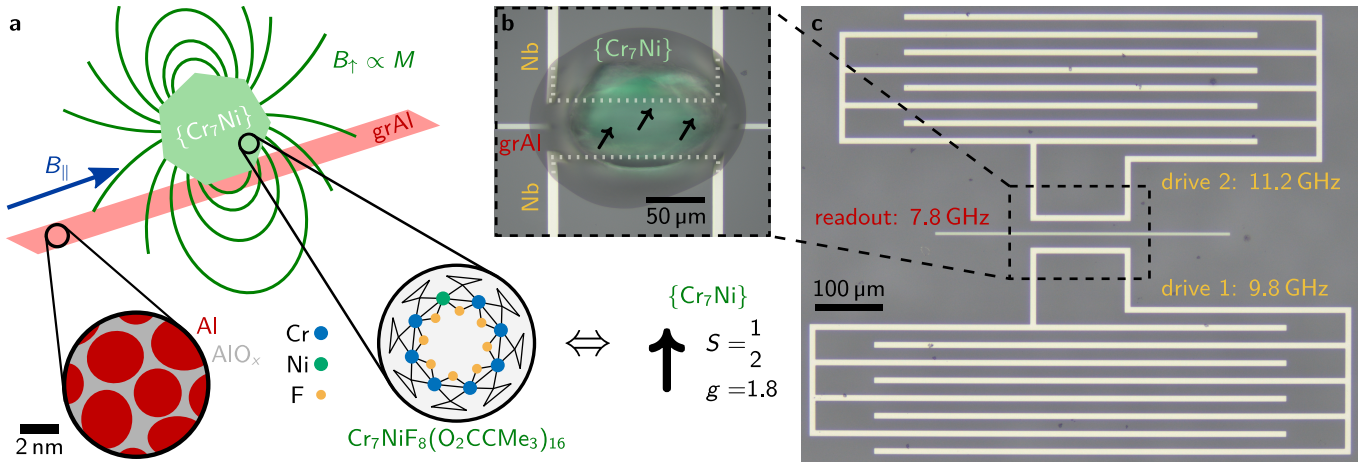


**FIG. 1. Implementation of kinetic inductance coupling between a superconducting resonator and molecular spins.** **a** Sketch of the resonator-spin system: high kinetic inductance granular aluminum (grAl) resonator (red strip) coupled to a  $\{\text{Cr}_7\text{Ni}\}$  micro-crystal (green). Left inset: grAl consists of crystalline aluminum grains (red) in an amorphous  $\text{AlO}_x$  matrix (gray) [32]. Right inset: the single magnetic molecule  $\text{Cr}_7\text{NiF}_8(\text{O}_2\text{CCMe}_3)_{16} \equiv \{\text{Cr}_7\text{Ni}\}$  has effective spin  $S = 1/2$  and  $g = 1.8$  [37, 38]. The magnetization of the spin ensemble due to in-plane field  $B_{\parallel}$  (blue arrow) creates a magnetic field  $B_{\uparrow}$  (green lines). This field locally enhances the kinetic inductance of the grAl resonator and provides the mechanism for longitudinal coupling. **b** Optical microscope image of the magnetic crystal (green) placed on top of the grAl readout resonator. The crystal is attached with *Apiezon N* [39] vacuum grease (transparent gray), which provides thermal conductivity at cryogenic temperatures, low levels of magnetic susceptibility and low microwave losses (cf. Appendix B). To excite the spins (black arrows) composing the crystal we use inductively coupled niobium lines, visible above and below the grAl resonator and shown as dashed white outlines in the region underneath the crystal. The 150  $\mu\text{m}$ -long inductor sections of the drive resonators parallel to the central grAl strip generate radio-frequency magnetic fields perpendicular to the spin quantization axis (defined by  $B_{\parallel}$ ). **c** Zoom-out: The grAl readout resonator (center) is flanked by two low-impedance niobium resonators (top, bottom), necessary to excite the spins. Note that the frequencies  $f_{\text{Nb},1}$ ,  $f_{\text{Nb},2}$  of the niobium drive resonators are several GHz detuned from the readout  $f_r$ .

to a superconducting fluxonium qubit.

Figure 1 illustrates the conceptual implementation of longitudinal coupling between a microwave resonator and a spin ensemble. The magnetic molecules are grown in a single crystal of chemically identical units, composed of eight chromium atoms with one substituted by nickel, which resemble cyclic wheels (cf. bottom right inset in Fig. 1a). Each molecule has an effective spin  $S = 1/2$  and gyromagnetic factor  $g \approx 1.8$  [37, 38, 40], chosen with  $g \neq 2$  in order to distinguish from spurious coupling to electronic spins in the environment of superconducting devices [25, 26, 29, 41]. The molecular crystal is placed at the center of a grAl stripline resonator with a resonance frequency  $f_r = 7.8$  GHz and internal quality factor  $Q_i > 10^5$  (cf. Appendix B). The grAl film has a kinetic inductance fraction  $\alpha \approx 1$  [30] (sheet inductance  $L_{\square} = 0.9$  nH  $\square^{-1}$ ) which arises from its microstructure, effectively forming a 3D network of JJs [32, 33, 42]. To drive the spin ensemble using microwave transverse fields, on the same chip (cf. Fig. 1b,c), we pattern two low impedance resonators ( $f_{\text{Nb},1} = 9.8$  GHz,  $f_{\text{Nb},2} = 11.2$  GHz) made of niobium, which can sustain relatively high current densities.

The longitudinal spin-resonator interaction arises from the coupling of the spin magnetic moments  $\mu = -g\mu_B\sigma_z/2$  to the resonator's kinetic inductance  $L_{\text{kin}}$ , where  $\mu_B$  denotes the Bohr magneton. The spin ensemble magnetization  $M$  increases  $L_{\text{kin}}$  and shifts the resonator

frequency  $f_r$  by  $\delta f_M$ :

$$\delta f_M/f_{r,0} \propto -M^2. \quad (1)$$

This frequency shift results from persistent currents  $I_p$  induced by the perpendicular component of the crystal field  $B_{\uparrow,\perp} \propto M$ . These currents locally increase the kinetic inductance  $L_{\text{kin}}(I_p) \approx L_{\text{kin},0}(1 + (I_p/I^*)^2)$ , where  $I^*$  characterizes the grAl nonlinearity and is typically on the order of the critical current [34, 43]. Given that the grAl effective penetration depth exceeds the resonator width by orders of magnitude [44, 45], we consider  $I_p \propto B_{\uparrow,\perp}$ . Note that the contribution of the superconducting gap suppression to  $\delta f_M$  is neglected, as the persistent current suppression dominates by 3 orders of magnitude for our resonator geometry [29].

Using the grAl resonator, in Fig. 2, we demonstrate the measurement of the  $\{\text{Cr}_7\text{Ni}\}$  crystal magnetization curve in parallel magnetic field  $B_{\parallel}$ . The observed frequency shift  $\delta f_r(B_{\parallel}, M)$  (cf. Fig. 2a) consists of two contributions: the shift  $\delta f_M$  from the crystal magnetization  $M$  (cf. Eq. (1)) and an additional parabolic frequency decrease due to the grAl gap suppression in  $B_{\parallel}$  [29]. To disentangle these effects, we fit the parabolic tail of the frequency shift  $\delta f_r(B_{\parallel}, M_S)$  in the field range where the ensemble magnetization is saturated ( $M = M_S$ ), specifically for  $B_{\parallel} > 0.32$  T in Fig. 2a. Subtracting the fitted parabolic response  $\delta f_r(B_{\parallel}, 0)$  (dashed line in Fig. 2a) from the measured data  $\delta f_r(B_{\parallel}, M)$  isolates the contri-

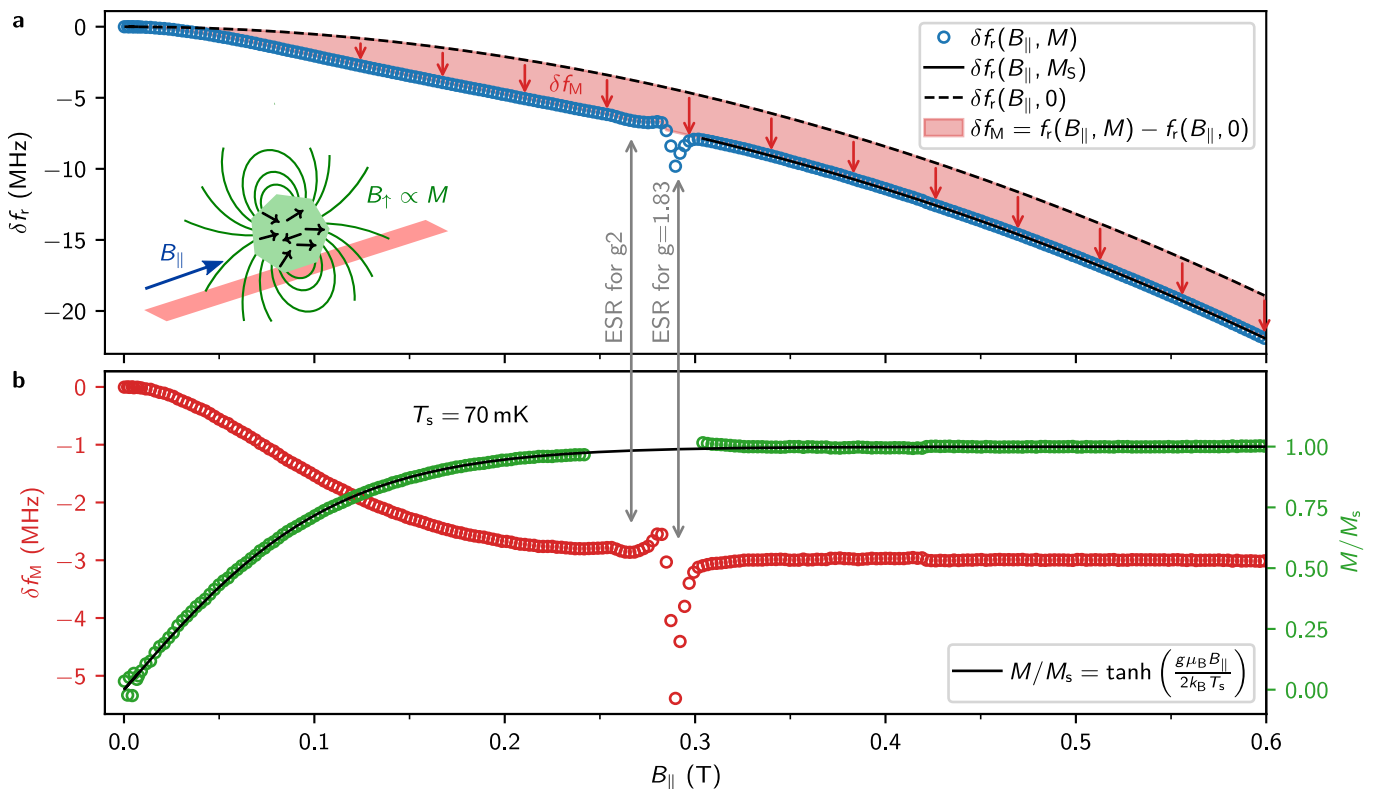


FIG. 2. **Detuning independent readout of the spin ensemble magnetization.** **a** Resonance frequency shift of the grAl readout resonator coupled to the molecular spin ensemble  $\delta f_r(B_{\parallel}, M)$  (blue markers) in magnetic field. The parabolic frequency shift of the bare resonator  $\delta f_r(B_{\parallel}, M = 0)$  (black dashed line) is given by the suppression of the grAl superconducting gap  $\delta(B_{\parallel})$  in magnetic field [29]. The resonator experiences an additional frequency shift  $\delta f_M$  due to the magnetization of the spin ensemble (red shift), yielding the measured total frequency shift  $\delta f_r(B_{\parallel}, M)$ . To disentangle these two contributions, we fit a parabolic frequency shift  $\delta f_r(B_{\parallel}, M_S)$  to the tail of the data for  $B_{\parallel} > 0.32$  T (black solid) where the magnetization of the crystal is saturated ( $M = M_S$ ). We can then remove the vertical offset to get  $\delta f_r(B_{\parallel}, 0)$  (dashed black) and  $\delta f_M$  (red arrows). At  $B_{\parallel} = 0.29$  T, as expected for  $g = 1.83$ , we measure an avoided level crossing due to the transverse coupling of the spin ensemble to the geometric inductance of the resonator. At  $B_{\parallel} = 0.26$  T we observe an additional feature corresponding to transverse coupling of  $g = 2$  spurious ESR [25, 26, 29, 41]. **b** Extracted frequency shift  $\delta f_M$  (red markers) due to the magnetic field of the crystal and corresponding magnetization  $M \propto \sqrt{\delta f_M}$  (green markers). Above  $B_{\parallel} = 0.32$  T, the crystal magnetization saturates, and  $\delta f_M$  remains constant. In the range  $B_{\parallel} = 0.244$ – $0.302$  T, anti-crossings (see double arrow markers) arising from residual transverse coupling to  $g = 2$  and  $g = 1.83$  spins prevent a reliable extraction of the magnetization. Note that the magnetization curve shown here is measured on a sample without Nb drive resonators (cf. Fig. 1) in order to avoid field distortions (cf. Appendix C).

bution  $\delta f_M$  from the crystal’s magnetization, shown in Fig. 2b. In addition, due to the resonator’s geometric inductance, near  $B_{\parallel} = 0.29$  T we observe small transverse couplings to the  $g = 1.83$  spins and to spurious  $g = 2$  spin impurities.

The magnetization curve in Fig. 2b, extracted from  $\delta f_M$  using Eq. (1), increases from  $M = 0$  to saturation  $M = M_S$  in fields above 300 mT. It follows the paramagnetic response  $M = M_S \tanh\left(\frac{g\mu_B B_{\parallel}}{2k_B T_S}\right)$  for a spin 1/2 ensemble, from which we fit a spin temperature of  $T_S = 70$  mK ( $k_B$  is the Boltzmann constant). Notably,  $T_S$  is above the cryostat temperature of  $T \approx 30$  mK, indicating limited thermalization of the molecular spin crystal via the vacuum grease (cf. Fig. 1). In a subsequent run with a smaller crystal, we extract a spin temperature of  $T_S = 30$  mK (cf. Appendix C), illustrating the challenge of thermalizing the ensemble - an issue commonly

referred to as the phonon bottleneck [46].

To conclude the spin ensemble characterization, we leverage the detuning-independent nature of kinetic inductance readout, which also remains effective during spin manipulation. As shown in Fig. 3a, we perform two-tone spectroscopy of the spins around 9.85 GHz, 2 GHz detuned from the readout resonator, and we measure  $g = 1.83 \pm 0.01$  (black dashed line), comparable to values reported in the literature [37, 40]. The excitation pattern reflects the expected convolution of the frequency dependent drive amplitude, shaped by the Nb resonators Lorentzian response, combined with the spin ensemble’s inhomogeneous linewidth.

On resonance with the Nb drive (red marker in Fig. 3a), we measure time-resolved excitation and decay of the ensemble magnetization (cf. Fig. 3b,c). We observe a non-exponential decay with  $1/e$  reached after

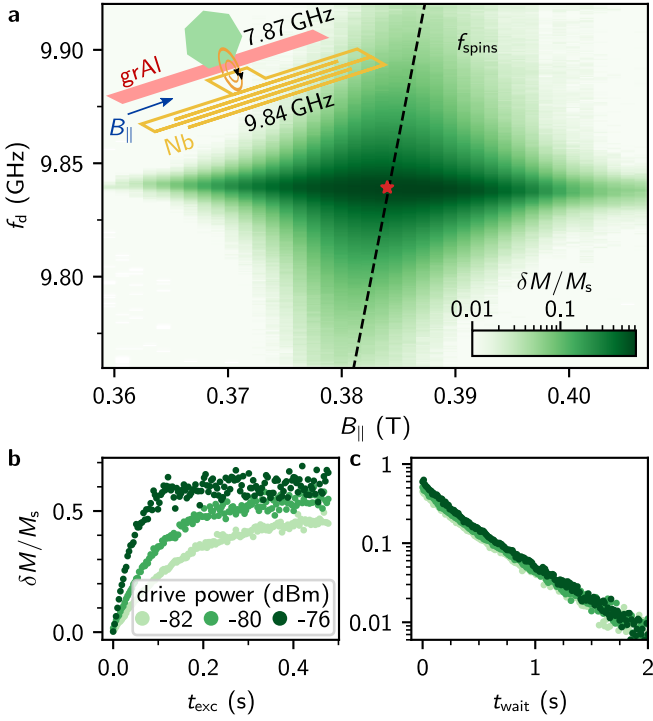


FIG. 3. **Excitation and decay of the spin ensemble 2 GHz detuned from the readout.** **a** Continuous wave two-tone spectroscopy of the spin ensemble: To excite the spins, we sweep a drive tone  $f_d$  in the vicinity of the niobium resonator frequency  $f_{\text{Nb1}} = 9.84$  GHz while monitoring the readout resonator at  $f_r = 7.87$  GHz. The relative change of the ensemble magnetization  $\delta M/M_S$  (green colorbar) is calibrated to the measured shift in  $f_r$  utilizing a magnetization curve (cf. Fig. 2b). The excitation of the spin ensemble is only effective within the bandwidth  $\kappa = 2$  MHz of the Nb drive resonator. The dashed line indicates the center frequency of the spin distribution given by  $hf = g\mu_B B_{\parallel}$  with  $g = 1.83 \pm 0.01$ . **b, c** Time domain characterization of the spin ensemble at  $B_{\parallel} = 0.384$  T (red marker in **a**): excitation to saturation (**b**) and decay from saturation (**c**) for different drive powers, with a  $1/e$  time  $\tau = 0.38$  s.

$\tau = 0.38$  s. This lifetime, significantly longer than reported for the same  $\{\text{Cr}_7\text{Ni}\}$  molecules in solution [38], is likely limited by the decay of the crystal phonons into the substrate (phonon bottleneck [46]), consistent with Ref. [47]. Note that we exclude drive induced heating as origin of the spin excitation, since the ensemble magnetization remains unchanged when the spins are detuned from the drive (e.g. at  $B_{\parallel} = 0.36$  T in Fig. 3a).

In Fig. 4, we propose a kinetic inductance coupling scheme for a single spin, utilizing established grAl circuit elements. To obtain longitudinal coupling to the highly localized dipole field of a single spin, we need to concentrate the kinetic inductance within a nanoscopic volume. This volume reduction inherently increases device nonlinearity [33], which for the 20 nm cross-section in Fig. 4a effectively results in a Josephson junction, referred to as a grAl nanojunction [42]. The spin dependent local magnetic field threading the nanojunction locally induces a quadratic suppression of the grAl super-

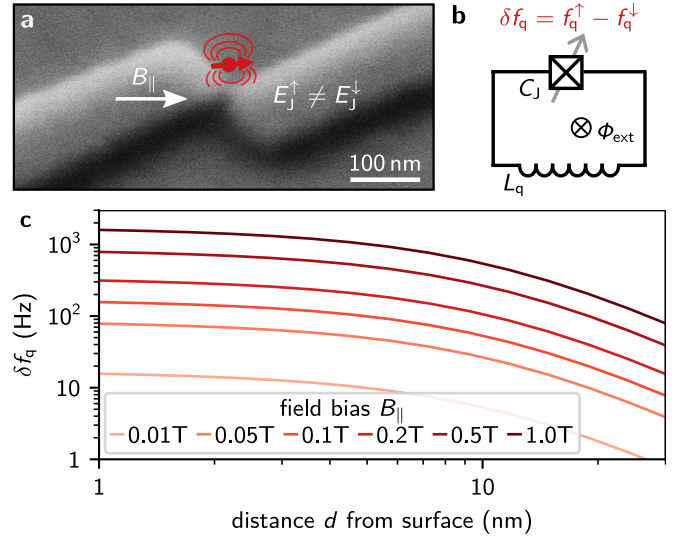


FIG. 4. **Towards longitudinal coupling between superconducting circuits and single spins.** **a** Implementation of a spin-modulated Josephson junction: scanning electron microscope image of a grAl nanojunction with a single spin sketched on top. The nanojunction consists of a  $\approx (20 \text{ nm})^3$  grAl volume [42], which remains coherent in Tesla-scale magnetic fields [41]. When biased in magnetic field  $B_{\parallel}$ , the two spin orientations generate different local magnetic fields, leading to distinct Josephson energies  $E_J^{\uparrow}$  and  $E_J^{\downarrow}$ . **b** We use the spin-state-dependent nanojunction to build a fluxonium quantum circuit with junction capacitance  $C_J$ , superinductor  $L_q$  and external flux  $\Phi_{\text{ext}}$ . The spin polarization tunes the Josephson energy  $E_J$  and, consequently, the fluxonium transition frequency  $f_q$ . **c** Simulation of the qubit frequency shift  $\delta f_q$  for a spin-flip versus distance  $d$  from the nanojunction surface for several  $B_{\parallel}$  bias values. Note that for the calculation we used a spin with magnetic moment  $\mu = 10\mu_B$  (see Ref. [15]) on top of a regular grAlmonium qubit [42].

conducting gap  $\Delta$ , resulting in a spin-state-dependent Josephson energy  $E_J$ :  $E_J^{\uparrow} \neq E_J^{\downarrow}$ .

We propose embedding the grAl nanojunction into a fluxonium quantum circuit operated at the half-flux sweet spot, where the qubit frequency is exponentially sensitive to variations in  $E_J$  [42]. The resulting circuit shown in Fig. 4b can be described by the standard fluxonium Hamiltonian

$$H_{\text{flux}} = 4ECn^2 + \frac{1}{2}E_L \left( \varphi - 2\pi \frac{\Phi_{\text{ext}}}{\Phi_0} \right)^2 - E_J \cos \varphi, \quad (2)$$

where  $E_L = (\Phi_0/2\pi)^2/L_q$  and  $EC = e^2/2C$  denote the fluxonium inductive and charging energies, respectively. Besides the trivial modulation from the bias field  $B_{\parallel}$ ,  $E_J = E_J(B_{\parallel}, \sigma_z)$  also depends on the spin qubit state  $\sigma_z$ , thereby implementing a longitudinal coupling where  $\sigma_z$  commutes with  $H_{\text{flux}}$ . A practical realization of such a circuit should be resilient to the high magnetic fields required for spin qubit operation, as recently demonstrated in a gradiometric geometry in Ref. [41].

To estimate the fluxonium qubit frequency shift  $\delta f_q$  due to a spin flip in a realistic scenario, we model the

spin as a point-like magnetic dipole with a magnetic moment  $\mu = 10\mu_B$  oriented (anti-) parallel to the bias field  $B_{\parallel}$ . Such spins can be engineered in single molecule magnets with strong anisotropy, forming an effective two-level-system with large magnetic moment [15]. For a spin centered at a distance  $d$  above the nanojunction, we numerically calculate the local grAl gap suppression  $\Delta(\vec{B}_{\uparrow}(\vec{r}) + \vec{B}_{\parallel})/\Delta(0) = \sqrt{1 - (|\vec{B}_{\uparrow}(\vec{r}) + \vec{B}_{\parallel}|/B_c)^2}$  [48] at position  $\vec{r}$  within its  $(20\text{ nm})^3$  volume. By numerically solving Eq. (2) for the corresponding  $E_J \propto \iiint d\vec{r}\Delta(\vec{r})$ , we find the qubit frequency shift  $\delta f_q$ , shown in Fig. 4c. Positioning the spin as close as possible to the nanojunction and operating in the  $B_{\parallel} \sim 10^2$  mT range enables spin-state-dependent frequency shifts  $\delta f_q$  on the order of kHz. Given that superconducting qubit frequencies can be resolved with kHz accuracy [49, 50], we are optimistic that longitudinal coupling via kinetic inductance will enable single shot QND readout of individual spins.

In conclusion, we have demonstrated longitudinal coupling between a  $\{\text{Cr}_7\text{Ni}\}$  molecular spin ensemble and a grAl superconducting microwave resonator via kinetic inductance, enabling frequency-independent and non-demolishing spin readout. The independence of the readout contrast on detuning between the spins and the resonator allowed us to measure the full magnetization curve

over a field range of hundreds of mT and observe time-resolved spin dynamics at GHz detuning. To overcome ensemble limitations like inhomogeneous broadening and the phonon relaxation bottleneck, we propose extending this longitudinal coupling scheme to a single spin positioned in the close vicinity of a grAl nanojunction in a fluxonium qubit. For state-of-the-art grAl devices, our simulations predict a spin-dependent qubit frequency shift up to kHz, opening the path for QND interaction at the single-spin level. Order of magnitude stronger interaction could be possible by miniaturizing the nanojunction by a factor of two and embedding the magnetic molecule in its center.

## ACKNOWLEDGEMENTS

We are grateful to Eufemio Moreno-Pineda and Kiril Borisov for fruitful discussions and we acknowledge technical support from S. Diewald and L. Radtke. Funding was provided by the German Research Foundation (DFG) via the Gottfried Wilhelm Leibniz-Award (ZVN-2020-WE 4458-5) and by the European Research Council via project number 101118911 (DarkQuantum). Facilities use was supported KIT Nanostructure Service Laboratory (NSL). We acknowledge qKit for providing a convenient measurement software framework.

- 
- [1] G. Burkard, T. D. Ladd, A. Pan, J. M. Nichol, and J. R. Petta, Semiconductor spin qubits, *Rev. Mod. Phys.* **95**, 025003 (2023).
  - [2] M. Zhong, M. P. Hedges, R. L. Ahlefeldt, J. G. Bartholomew, S. E. Beavan, S. M. Wittig, J. J. Longdell, and M. J. Sellars, Optically addressable nuclear spins in a solid with a six-hour coherence time, *Nature* **517**, 177 (2015).
  - [3] D. Serrano, S. K. Kuppusamy, B. Heinrich, O. Fuhr, D. Hunger, M. Ruben, and P. Goldner, Ultra-narrow optical linewidths in rare-earth molecular crystals, *Nature* **603**, 241 (2022).
  - [4] J. O’Sullivan, J. Travesedo, L. Pallegoix, Z. W. Huang, A. May, B. Yavkin, P. Hogan, S. Lin, R. Liu, T. Chanelliere, S. Bertaina, P. Goldner, D. Esteve, D. Vion, P. Abgrall, P. Bertet, and E. Flurin, Individual solid-state nuclear spin qubits with coherence exceeding seconds, arXiv 10.48550/arXiv.2410.10432 (2024), 2410.10432.
  - [5] G. Kurizki, P. Bertet, Y. Kubo, K. Mølmer, D. Petrosyan, P. Rabl, and J. Schmiedmayer, Quantum technologies with hybrid systems, *Proc. Natl. Acad. Sci. U.S.A.* **112**, 3866 (2015).
  - [6] Z.-L. Xiang, S. Ashhab, J. Q. You, and F. Nori, Hybrid quantum circuits: Superconducting circuits interacting with other quantum systems, *Rev. Mod. Phys.* **85**, 623 (2013).
  - [7] A. A. Clerk, K. W. Lehnert, P. Bertet, J. R. Petta, and Y. Nakamura, Hybrid quantum systems with circuit quantum electrodynamics, *Nat. Phys.* **16**, 257 (2020).
  - [8] Y. Kubo, F. R. Ong, P. Bertet, D. Vion, V. Jacques, D. Zheng, A. Dréau, J.-F. Roch, A. Auffeves, F. Jelezko, J. Wrachtrup, M. F. Barthe, P. Bergonzo, and D. Esteve, Strong Coupling of a Spin Ensemble to a Superconducting Resonator, *Phys. Rev. Lett.* **105**, 140502 (2010).
  - [9] D. I. Schuster, A. P. Sears, E. Ginossar, L. DiCarlo, L. Frunzio, J. J. L. Morton, H. Wu, G. A. D. Briggs, B. B. Buckley, D. D. Awschalom, and R. J. Schoelkopf, High-Cooperativity Coupling of Electron-Spin Ensembles to Superconducting Cavities, *Phys. Rev. Lett.* **105**, 140501 (2010).
  - [10] A. Bienfait, J. J. Pla, Y. Kubo, M. Stern, X. Zhou, C. C. Lo, C. D. Weis, T. Schenkel, M. L. W. Thewalt, D. Vion, D. Esteve, B. Julsgaard, K. Mølmer, J. J. L. Morton, and P. Bertet, Reaching the quantum limit of sensitivity in electron spin resonance, *Nat. Nanotechnol.* **11**, 253 (2016).
  - [11] C. Eichler, A. J. Sigillito, S. A. Lyon, and J. R. Petta, Electron Spin Resonance at the Level of  $10^4$  Spins Using Low Impedance Superconducting Resonators, *Phys. Rev. Lett.* **118**, 037701 (2017).
  - [12] C. Bonizzoni, A. Ghirri, M. Atzori, L. Sorace, R. Sessoli, and M. Affronte, Coherent coupling between Vanadyl Phthalocyanine spin ensemble and microwave photons: towards integration of molecular spin qubits into quantum circuits, *Sci. Rep.* **7**, 1 (2017).
  - [13] M. Mergenthaler, J. Liu, J. J. Le Roy, N. Ares, A. L. Thompson, L. Bogani, F. Luis, S. J. Blundell, T. Lancaster, A. Ardavan, G. A. D. Briggs, P. J. Leek, and E. A. Laird, Strong Coupling of Microwave Photons to

- Antiferromagnetic Fluctuations in an Organic Magnet, *Phys. Rev. Lett.* **119**, 147701 (2017).
- [14] I. Gimeno, W. Kersten, M. C. Pallarés, P. Hermosilla, M. J. Martínez-Pérez, M. D. Jenkins, A. Angerer, C. Sánchez-Azqueta, D. Zueco, J. Majer, A. Lostao, and F. Luis, Enhanced Molecular Spin-Photon Coupling at Superconducting Nanoconstrictions, *ACS Nano* **14**, 8707 (2020).
- [15] E. Moreno-Pineda and W. Wernsdorfer, Measuring molecular magnets for quantum technologies, *Nat. Rev. Phys.* **3**, 645 (2021).
- [16] Z. Wang, L. Balembois, M. Rančić, E. Billaud, M. Le Dantec, A. Ferrier, P. Goldner, S. Bertaina, T. Chanelière, D. Esteve, D. Vion, P. Bertet, and E. Flurin, Single-electron spin resonance detection by microwave photon counting, *Nature* **619**, 276 (2023).
- [17] A. Bienfait, J. J. Pla, Y. Kubo, X. Zhou, M. Stern, C. C. Lo, C. D. Weis, T. Schenkel, D. Vion, D. Esteve, J. J. L. Morton, and P. Bertet, Controlling spin relaxation with a cavity, *Nature* **531**, 74 (2016).
- [18] A. Blais, A. L. Grimsmo, S. M. Girvin, and A. Wallraff, Circuit quantum electrodynamics, *Rev. Mod. Phys.* **93**, 025005 (2021).
- [19] M. F. Dumas, B. Groleau-Paré, A. McDonald, M. H. Muñoz-Arias, C. Lledó, B. D'Anjou, and A. Blais, Measurement-Induced Transmon Ionization, *Phys. Rev. X* **14**, 041023 (2024).
- [20] N. Didier, J. Bourassa, and A. Blais, Fast Quantum Non-demolition Readout by Parametric Modulation of Longitudinal Qubit-Oscillator Interaction, *Phys. Rev. Lett.* **115**, 203601 (2015).
- [21] S. Richer and D. DiVincenzo, Circuit design implementing longitudinal coupling: A scalable scheme for superconducting qubits, *Phys. Rev. B* **93**, 134501 (2016).
- [22] R. Dassonneville, T. Ramos, V. Milchakov, L. Planat, É. Dumur, F. Foroughi, J. Puertas, S. Leger, K. Bhargava, J. Delaforce, C. Naud, W. Hasch-Guichard, J. J. García-Ripoll, N. Roch, and O. Buisson, Fast High-Fidelity Quantum Nondemolition Qubit Readout via a Nonperturbative Cross-Kerr Coupling, *Phys. Rev. X* **10**, 011045 (2020).
- [23] A. A. Chapple, A. McDonald, M. H. Muñoz-Arias, and A. Blais, Robustness of longitudinal transmon readout to ionization, arXiv [10.48550/arXiv.2412.07734](https://arxiv.org/abs/10.48550/arXiv.2412.07734) (2024), [2412.07734](https://arxiv.org/abs/2412.07734).
- [24] W. Wernsdorfer, From micro- to nano-SQUIDS: applications to nanomagnetism, *Supercond. Sci. Technol.* **22**, 064013 (2009).
- [25] J. G. Kroll, F. Borsoi, K. L. van der Enden, W. Uilhoorn, D. de Jong, M. Quintero-Pérez, D. J. van Woerkom, A. Bruno, S. R. Plissard, D. Car, E. P. A. M. Bakkers, M. C. Cassidy, and L. P. Kouwenhoven, Magnetic-Field-Resilient Superconducting Coplanar-Waveguide Resonators for Hybrid Circuit Quantum Electrodynamics Experiments, *Phys. Rev. Appl.* **11**, 064053 (2019).
- [26] N. Samkharadze, A. Bruno, P. Scarlino, G. Zheng, D. P. DiVincenzo, L. DiCarlo, and L. M. K. Vandersypen, High-Kinetic-Inductance Superconducting Nanowire Resonators for Circuit QED in a Magnetic Field, *Phys. Rev. Appl.* **5**, 044004 (2016).
- [27] A. Bahr, M. Boselli, B. Huard, and A. Bienfait, Improving magnetic-field resilience of NbTiN planar resonators using a hard-mask fabrication technique, *Appl. Phys. Lett.* **124**, [10.1063/5.0191393](https://doi.org/10.1063/5.0191393) (2024).
- [28] T. Charpentier, D. Perconte, S. Léger, K. R. Amin, F. Blondelle, F. Gay, O. Buisson, L. Ioffe, A. Khvalyuk, I. Poboiko, M. Feigel'man, N. Roch, and B. Sacépé, First-order quantum breakdown of superconductivity in an amorphous superconductor, *Nat. Phys.* **21**, 104 (2025).
- [29] K. Borisov, D. Rieger, P. Winkel, F. Henriques, F. Valenti, A. Ionita, M. Wessbecher, M. Spiecker, D. Gusenkova, I. M. Pop, and W. Wernsdorfer, Superconducting granular aluminum resonators resilient to magnetic fields up to 1 tesla, *Applied Physics Letters* **117**, [120502](https://doi.org/10.1063/5.0018012) (2020), <https://doi.org/10.1063/5.0018012>.
- [30] L. Grünhaupt, N. Maleeva, S. T. Skacel, M. Calvo, F. Levy-Bertrand, A. V. Ustinov, H. Rotzinger, A. Monfardini, G. Catelani, and I. M. Pop, Loss Mechanisms and Quasiparticle Dynamics in Superconducting Microwave Resonators Made of Thin-Film Granular Aluminum, *Phys. Rev. Lett.* **121**, 117001 (2018).
- [31] I. Siddiqi, Engineering high-coherence superconducting qubits, *Nat. Rev. Mater.* **6**, 875 (2021).
- [32] G. Deutscher, H. Fenichel, M. Gershenson, E. Grünbaum, and Z. Ovadyahu, Transition to zero dimensionality in granular aluminum superconducting films, *J. Low Temp. Phys.* **10**, 231 (1973).
- [33] N. Maleeva, L. Grünhaupt, T. Klein, F. Levy-Bertrand, O. Dupre, M. Calvo, F. Valenti, P. Winkel, F. Friedrich, W. Wernsdorfer, A. V. Ustinov, H. Rotzinger, A. Monfardini, M. V. Fistul, and I. M. Pop, Circuit quantum electrodynamics of granular aluminum resonators, *Nat. Commun.* **9**, 1 (2018).
- [34] J. Luomahaara, V. Vesterinen, L. Grönberg, and J. Hassel, Kinetic inductance magnetometer, *Nat. Commun.* **5**, 1 (2014).
- [35] A. T. Asfaw, E. I. Kleinbaum, T. M. Hazard, A. Gyenis, A. A. Houck, and S. A. Lyon, SKIFFS: Superconducting Kinetic Inductance Field-Frequency Sensors for sensitive magnetometry in moderate background magnetic fields, *Appl. Phys. Lett.* **113**, [10.1063/1.5049615](https://doi.org/10.1063/1.5049615) (2018).
- [36] S. Sypkens, F. Faramarzi, M. Colangelo, A. Sinclair, R. Stephenson, and J. Glasby, Development of an Array of Kinetic Inductance Magnetometers (KIMs), *IEEE Trans. Appl. Supercond.* **31**, ArticleSequenceNumber:2400104 (2021).
- [37] F. K. Larsen, E. J. L. McInnes, H. E. Mkami, J. Overgaard, S. Piligkos, G. Rajaraman, E. Rentschler, A. A. Smith, G. M. Smith, V. Boote, M. Jennings, G. A. Timco, and R. E. P. Winpenny, Synthesis and Characterization of Heterometallic {Cr7M} Wheels, *Angew. Chem.* **115**, 105 (2003).
- [38] A. Ardavan, O. Rival, J. J. L. Morton, S. J. Blundell, A. M. Tyryshkin, G. A. Timco, and R. E. P. Winpenny, Will Spin-Relaxation Times in Molecular Magnets Permit Quantum Information Processing?, *Phys. Rev. Lett.* **98**, 057201 (2007).
- [39] *Apiezon N Grease* (2024), [Online; accessed 15. Apr. 2024].
- [40] G. A. Timco, S. Carretta, F. Troiani, F. Tuna, R. J. Pritchard, C. A. Muryn, E. J. L. McInnes, A. Ghirri, A. Candini, P. Santini, G. Amoretti, M. Affronte, and R. E. P. Winpenny, Engineering the coupling between molecular spin qubits by coordination chemistry, *Nat. Nanotechnol.* **4**, 173 (2009).
- [41] S. Günzler, J. Beck, D. Rieger, N. Gosling, N. Zapata, M. Field, S. Geisert, A. Bacher, J. K. Hohmann,

- M. Spiecker, W. Wernsdorfer, and I. M. Pop, Spin Environment of a Superconducting Qubit in High Magnetic Fields, arXiv [10.48550/arXiv.2501.03661](https://arxiv.org/abs/10.48550/arXiv.2501.03661) (2025), [2501.03661](https://arxiv.org/abs/10.48550/arXiv.2501.03661).
- [42] D. Rieger, S. Günzler, M. Spiecker, P. Paluch, P. Winkel, L. Hahn, J. K. Hohmann, A. Bacher, W. Wernsdorfer, and I. M. Pop, Granular aluminium nanojunction fluxonium qubit, *Nat. Mater.* **22**, 194 (2023).
- [43] B. Ho Eom, P. K. Day, H. G. LeDuc, and J. Zmuidzinas, A wideband, low-noise superconducting amplifier with high dynamic range, *Nat. Phys.* **8**, 623 (2012).
- [44] D. Abraham, G. Deutscher, R. Rosenbaum, and S. Wolf, Characteristics of granular Al-Al<sub>2</sub>O<sub>3</sub> SQUIDs, *J. Low Temp. Phys.* **32**, 853 (1978).
- [45] M. Gershenson and W. L. McLean, Magnetic susceptibility of superconducting granular aluminum, *J. Low Temp. Phys.* **47**, 123 (1982).
- [46] I. Chiorescu, W. Wernsdorfer, A. Müller, H. Bögge, and B. Barbara, Butterfly Hysteresis Loop and Dissipative Spin Reversal in the  $S = 1/2$ ,  $V_{15}$  Molecular Complex, *Phys. Rev. Lett.* **84**, 3454 (2000).
- [47] W. Wernsdorfer, D. Mailly, G. A. Timco, and R. E. P. Wippeny, Resonant photon absorption and hole burning in Cr<sub>7</sub>Ni antiferromagnetic rings, *Phys. Rev. B* **72**, 060409 (2005).
- [48] D. H. Douglass, Magnetic Field Dependence of the Superconducting Energy Gap, *Phys. Rev. Lett.* **6**, 346 (1961).
- [49] J. J. Burnett, A. Bengtsson, M. Scigliuzzo, D. Niepce, M. Kudra, P. Delsing, and J. Bylander, Decoherence benchmarking of superconducting qubits, *npj Quantum Inf.* **5**, 1 (2019).
- [50] A. Somoroff, Q. Ficheux, R. A. Mencia, H. Xiong, R. Kuzmin, and V. E. Manucharyan, Millisecond Coherence in a Superconducting Qubit, *Phys. Rev. Lett.* **130**, 267001 (2023).
- [51] D. Rieger, S. Günzler, M. Spiecker, A. Nambisan, W. Wernsdorfer, and I. M. Pop, Fano Interference in Microwave Resonator Measurements, *Phys. Rev. Appl.* **20**, 014059 (2023).
- [52] V. Gupta, P. Winkel, N. Thakur, P. van Vlaanderen, Y. Wang, S. Ganjam, L. Frunzio, and R. J. Schoelkopf, Low loss lumped-element inductors made from granular aluminum, arXiv [10.48550/arXiv.2411.12611](https://arxiv.org/abs/10.48550/arXiv.2411.12611) (2024), [2411.12611](https://arxiv.org/abs/10.48550/arXiv.2411.12611).

## APPENDICES

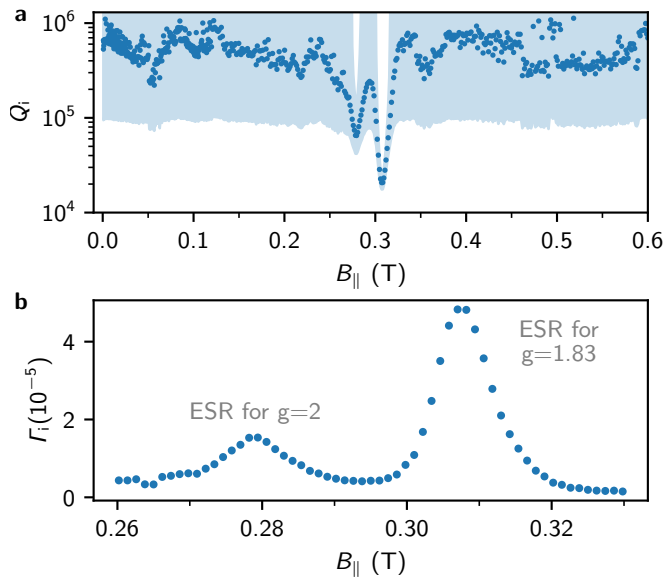


FIG. 5. **Resilience of grAl resonators in parallel field.** Internal quality factor  $Q_i$  (blue markers) corresponding Fano uncertainty range [51] (blue shaded area) of the grAl resonator in magnetic field  $B_{\parallel}$ . The resonator is measured at an average photon number  $\bar{n} \approx 10$  with a coupling quality factor  $Q_c = 25 \times 10^3$ . The dips in  $Q_i$ , shown as peaks in the decay rate  $\Gamma_i = 1/Q_i$  in (b), correspond to ESR of spurious electronic spins with  $g = 2$  (left) and the molecular spin ensemble with  $g = 1.83$  (right). The associated resonance frequency shifts are presented in Fig. 6.

#### Appendix A: Fabrication details

The resonators discussed in this manuscript are fabricated on a double-side-polished c-plane sapphire substrate. They are patterned using lift-off optical lithography with AZ5214E photoresist, followed by development in AZ developer. Before metal deposition, an Ar/O<sub>2</sub> plasma cleaning step is performed using a Kaufman ion source. Additionally, a titanium gettering step reduces the chamber pressure to  $p \sim 10^{-7}$  mbar before evaporation in a Plassys MEB 550S shadow evaporation system. The 20 nm granular aluminum (grAl) film is deposited at 1 nm/s, yielding a sheet resistance of 1.1 k $\Omega$ / $\square$ . In a second lithography step, 50 nm thick niobium drive resonators are patterned and deposited with an evaporation rate of 1 nm/s, using the same optical procedure.

#### Appendix B: grAl resonator in magnetic field

In Fig. 5, we confirm the resilience of the grAl readout resonator in parallel magnetic field  $B_{\parallel}$ . The internal quality factor remains above  $Q_i \gtrsim 10^5$ , even when

accounting for systematic Fano uncertainty in the loss measurement [51], except for two distinct dips. These increased losses occur where the resonator frequency matches the ESR of the  $g = 1.83$  molecular spin ensemble and of spurious  $g = 2$  spins, commonly observed in the environment of superconducting devices [25, 26, 29, 41]. The latter can serve as an in-situ calibration of the on-chip magnetic field strength.

Notably, the quality factors of the grAl resonator are not affected by the *Apiezon N* [39] vacuum grease on top, used to thermalize and attach the crystal (cf. Fig. 1). Within the uncertainty, the values reported in Fig. 5 are equivalent to values reported in the literature [29, 30, 51] and could be further improved by an order of magnitude for optimized geometry, substrate and cleaning procedures, as shown in Ref. [52].

Beyond field strength, we also calibrate the field direction to ensure that all measurements in this manuscript are performed with  $B_{\parallel}$  strictly aligned with the substrate plane. This prevents hysteretic, non-monotonic resonance frequency shifts and additional perpendicular field ( $B_{\perp}$ ) effects that would complicate the extraction of  $\delta f_M$ . To compensate for minor chip misalignments within our cylindrical sample holder (identical to Refs. [29, 41, 51]) we introduce an out-of-plane compensation field  $B_{\perp, \text{comp}}$  for each applied  $B_{\parallel}$ . We determine  $B_{\perp, \text{comp}}$  by sweeping the perpendicular field component  $B_{\perp}$  and maximizing the resonator frequency.

#### Appendix C: Additional magnetization curve

In Fig. 6, we confirm that the presence of the Nb drive resonators, which introduces magnetic field distortions, still allows reliable extraction of the spin ensemble magnetization. As shown in Fig. 1, these Nb resonators are patterned directly adjacent to the grAl readout resonator. The extracted shift  $\delta f_M$  and corresponding magnetization  $M$ , shown in Fig. 6b, exhibit saturation behavior similar to the sample without Nb resonators (cf. Fig. 2). The frequency shift at saturation  $\delta f_M(M_S)$  is smaller compared to Fig. 2 due to the use of a smaller molecular crystal. From a fit to the paramagnetic response  $M = M_S \tanh(\frac{g\mu_B B_{\parallel}}{2k_B T_S})$  for a spin 1/2 ensemble, we extract a spin temperature of  $T_S = 30$  mK. We attribute the lower spin temperature compared to Fig. 2 to the higher surface-to-volume-ratio of the smaller crystal, which enhances phonon decay into the substrate. For bias fields above  $B_{\parallel} > 300$  mT, the magnetization remains constant, but an additional shift in  $\delta f_M$  arises due to out-of-plane magnetic fields generated by screening currents in the niobium structures of the drive resonators.



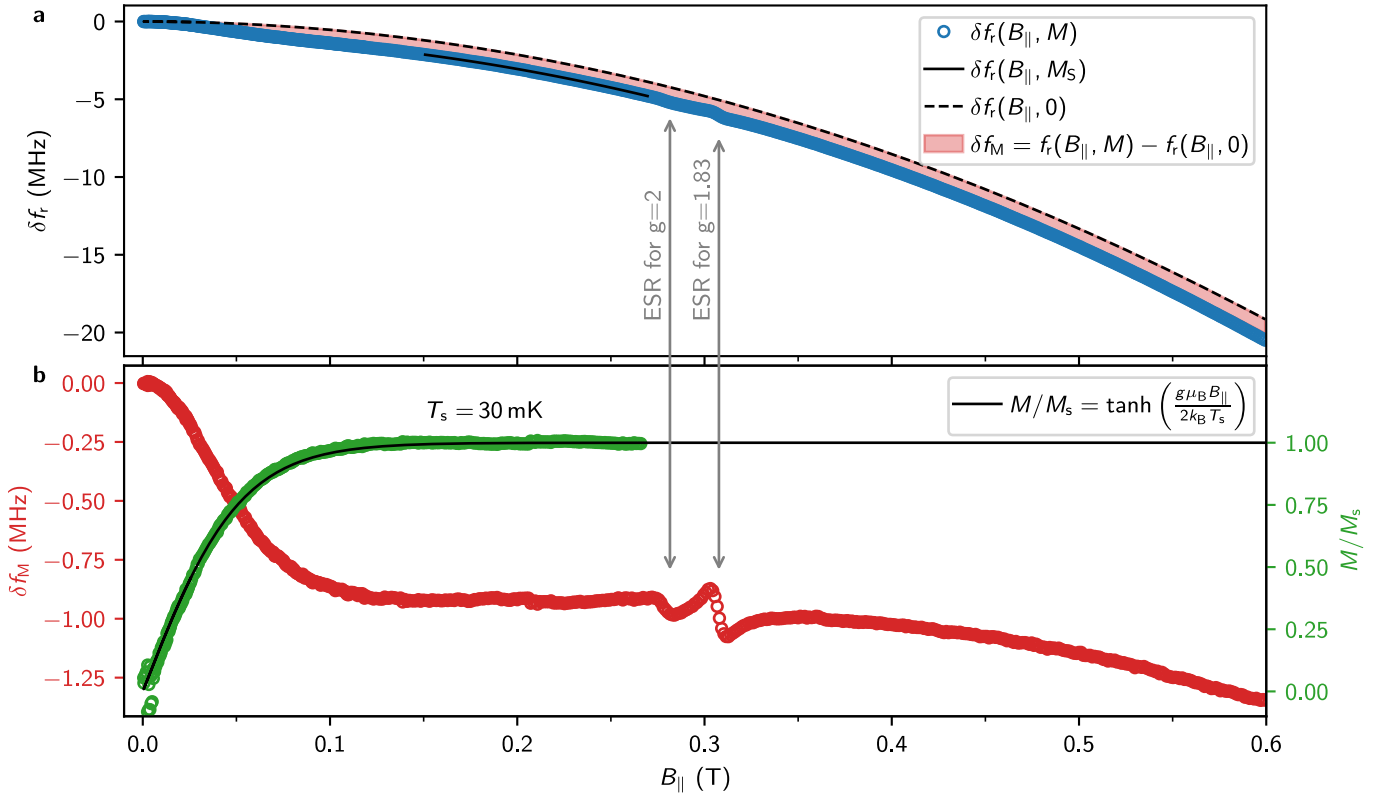


FIG. 6. **Readout of the spin ensemble magnetization in the presence of on-chip Nb drive resonators.** **a** Resonance frequency shift  $\delta f_r(B_{\parallel}, M)$  (blue markers) of the grAl readout resonator coupled to the molecular spin ensemble, measured in the presence of Nb drive resonators (which remain undriven during this measurement). To extract the magnetization  $M \propto \sqrt{\delta f_M}$  (green markers) in **b**, we fit the parabolic frequency shift  $\delta f_r(B_{\parallel}, M_S)$  for saturated spin crystal magnetization ( $M = M_S$ ) in the range  $B_{\parallel} = 150\text{--}270$  mT and follow the main text procedure (cf. Fig. 2). For fields above  $B_{\parallel} = 0.27$  T, as shown by the frequency shift  $\delta f_M$  (red markers) in **b**, anti-crossings arising from residual transverse coupling to  $g = 2$  and  $g = 1.83$  spins (gray arrows) as well as screening fields from the superconducting Nb structures distort the extracted frequency shift  $\delta f_M$ .